CrossMark

Unsteady-State Horizontal Solidification of an Al–Si–Cu–Fe Alloy: Relationship Between Thermal Parameters and Microstructure with Mechanical Properties/Fracture Feature

Fabricio A. Souza[2] · Igor A. Magno[2] · Marlo O. Costa[2] · André S. Barros[2] · Jacson M. Nascimento[2] · Diego B. Carvalho[1] · Otávio L. Rocha[1,2]

Abstract

Aluminum casting alloys have properties which are of great industrial interest, such as low density, good corrosion resistance, high thermal and electrical conductivities, good combination of mechanical properties, good workability in machining processes and mechanical forming. Currently, these alloys are produced in various systems and dozens of compositions. In this investigation, a mutual interaction of thermal parameters, scale of the dendritic microstructure, intermetallic compounds (IMCs), microhardness and tensile properties/fracture characteristics of a casting Al–7wt%Si–3wt%Cu–0.3wt%Fe alloy was analyzed. Solidification experiments were developed using a furnace that promoted horizontal growth under transient heat flow conditions. Then, growth rate (V_L), cooling rate (C_R), and local solidification time (t_{SL}) were determined from measured temperature profiles. Secondary dendritic spacings (λ_2), Si particles, Fe-rich and Al_2Cu intermetallic phases were characterized by optical and SEM microscopy, as well as the area mapping and point-wise EDS microanalysis. Hence, the interrelations involving Vickers microhardness (HV), yield strength (σ_{YS}), ultimate tensile strength (σ_{UTS}) and elongation (E%) with microstructural features were evaluated by mathematical equations. IMCs as well as morphologies of Si were also analyzed in the fracture regions. In addition, the experimental growth law of $\lambda_2 = f(t_{SL})$ proposed in this study was compared with a predictive theoretical model reported in the literature for multicomponent alloys. It was observed that areas that tend to grow faster (lowest λ_2 values) were associated with the highest σ_{UTS} and E% values, while HV and σ_{YS} properties were not affected by the thermal and microstructural parameters (C_R and λ_2). In addition, less extensive cleavage planes accompanied by small dimples in were observed in fractured samples with lower λ_2 values.

Keywords AlSiCuFe multicomponent alloys · Horizontal solidification · Thermal and microstructural parameters · Mechanical properties

1 Introduction

Aluminum-based alloys are materials of the highest potential of application in the aerospace and automotive industries, among which stand out the Al-Si casting alloys (which constitute 85%–90% of all aluminum alloys), mainly due to their superior castability characteristics. Material properties such as tensile strength, corrosion behavior, and ductility have been rigorously demanded by these applications and thus a greater control of the microstructure during the preparation of alloys and during solidification and/or heat treatment practices have been increasingly required.

In the case of preparation of alloys, the combination of various properties depends on the addition of alloying elements in the aluminum matrix. The alloying elements may be of various types, such as major and minor alloying elements, modifying agents, and impurity elements [1–3]. The addition of Cu in Al–Si alloys has shown to improve tensile strength by θ-Al_2Cu intermetallic phase precipitation, but has deleteriously affected corrosion resistance [4–6]. With regard to the solidification process, it is very important to control the microstructure, especially the Al_2Cu and

✉ Otávio L. Rocha
  otavio.rocha@ifpa.edu.br

1 Federal Institute of Education, Science and Technology
   of Pará - IFPA, Belém, PA 66093-020, Brazil

2 Faculty of Mechanical Engineering, Federal University
   of Pará - UFPA, Belém, PA 66075-110, Brazil

Si morphologies. In Al–Si cast alloys, Si can be present in the plate or lamellar, fibrous and spheroidal type morphologies, and Al_2Cu intermetallic phase can also be present in different shapes, as compact blocky-like phase, as eutectic phase, or as a mixture of both types [7, 8]. The presence in the microstructure of one or more forms of these phases is influenced by the solidification thermal parameters (V_L, C_R and t_{SL}) or by chemical modifying agents (such as Sr) or by the combined action of both process [5]. It can be observed that coarse plate-like Si particles have deleterious effects on ductility [7, 8].

Samuel et al. [9], analyzing 319 alloys solidified in higher C_R values conditions, have observed the eutectic Al_2Cu phase and a larger fraction of the blocky Al_2Cu phase when the alloy was subjected to modification by Sr. It has been also observed that addition of Mg in Al–Si–Cu alloys resulted in large amounts of the coarse blocky-like phase, compared to the finer eutectic-like form [10–14]. Although the isolated influence of Al_2Cu types on the mechanical properties is not yet known, their effects on solution heat treatment are being investigated in the literature. It has shown that the blocky Al_2Cu phase is more difficult to dissolve in the Al matrix [11–14].

The solidification thermal parameters (STP) have a direct influence on the formation of dendritic microstructures, as well as on the shape, size and distribution of the phases that form during the complex transformations that occur in Al–Si–Cu–Fe alloys. The cooling rate, the most critical parameter, is also the most studied in the literature since high C_R values result in lower dendrite arm spacing [15–37]. This has allowed a better control in the size and distribution of intermetallic phases and thus better properties [7]. For several decades, theoretical and experimental investigations on the correlation of STP with dendritic spacing have been elaborated for binary aluminum alloys [15–27], and more recently for multicomponent alloys [7, 28–34]. Among such studies, it is highlighted the works of Bouchard and Kirkaldy (BK) [16] as well as of Rappaz and Boetingger (RB) [34], which proposed mathematical models of secondary dendrite arm spacing (λ_2) growth for binary and multicomponent alloys, respectively. In the BK′ and RB′ models the λ_2 growth is conducted by V_L and t_{SL}, respectively. It can be seen that in the directional solidification, t_{SL} can be related to C_R in the form $t_{SL} = \Delta T/C_R$ [32], where ΔT is the solidification interval in the non-equilibrium conditions. The mathematical equations of the respective models are given by the following general expressions: $\lambda_2(BK) = \text{constant1} \cdot (V_L)^{-2/3}$ and $\lambda_2(RB) = \text{constant} \cdot (t_{SL})^{1/3}$, where constants 1, 2 are strictly controlled by the thermophysical properties of the investigated alloys. For binary Al–Si and Al–Cu alloys, several studies [4, 5, 15–18, 20–27, 33] have been developed and the experimental results have confirmed the λ_2 variation with V_L, C_R and t_{SL} with indexes equal to $-2/3$, $-1/3$

and 1/3, i.e., $\lambda_2 \, \alpha (V_L)^{-2/3}$, $\lambda_2 \, \alpha (C_R)^{-1/3}$ and $\lambda_2 \, \alpha (t_{SL})^{1/3}$. This has also been verified for multicomponent Al-based alloys [6–10, 12–14, 32–37].

Once the correlation between thermal and microstructural parameters is established during the solidification process, for example $\lambda_2 = f(STP)$, the influence of these parameters on the mechanical properties can also be analyzed. This has been extensively explored in the literature for binary aluminum-based alloys. On the other hand, investigations of this nature with multicomponent alloys are scarce. In this sense, recently published works on directional solidification of multicomponent aluminum alloys have been elaborated, which have proposed to the literature experimental laws relating microhardness and tensile strength with V_L, C_R and λ_2 [11–14, 28].

In the study of Brito et al. [28], upward directional solidification experiments were performed with Al–3wt%Mg and Al–3wt%Mg–1wt%Si alloys. The authors observed that the addition of Si in the binary AlMg alloy resulted in the formation of a complex arrangement of phases, including binary (α-Al + Mg_2Si) and refined ternary (α-Al + Mg_2Si + AlFe(Si)) eutectic mixtures and, as consequence, higher HV values were found for the multicomponent alloy. Hall–Petch equations of type $HV = 17 - 1350$ $(\lambda_2) + 415(\lambda_2)^{-1/2}$ and $HV = 91 - 94.6(\lambda_2)^{-1/2}$ were proposed for Al–3wt%Mg and Al–3wt%Mg–1wt%Si alloys, respectively. For both alloys, HV increased with the increase of λ_2.

Chen et al. [29] have analyzed solidification and heat treatment conditions for Al–7wt%Si–Xwt%Mg alloys and, unlike the results of Brito et al. [28], the tensile properties (σ_{YS} and σ_{UTS}) of the as-cast and heat treated samples increased with the decrease of λ_2. In addition, Chen et al. [29] have observed that high C_R values have influenced the dendritic microstructure (α-Al) with smaller λ_2 values, as well as the size and morphology of the silicon and intermetallic particles. For as-cast samples, the dependence of (σ_{YS} and σ_{UTS}) = $f(\lambda_2)$ has been represented by the following mathematical expressions: $\sigma_{YS} = -0.0041(\lambda_2)^2 + 0.118(\lambda_2) + 111.1$ and $\sigma_{UTS} = -0.029(\lambda_2)^2 + 1.72(\lambda_2) + 155.8$. It has been observed that higher σ_{YS} and σ_{UTS} values were found for heat treated samples.

In an investigation developed by Costa et al. [30], samples of the upward directionally solidified and T6 heat-treated Al–5.5wt%Si–3wt%Cu alloy were evaluated. The results showed that the levels of cooling rates experienced during solidification allowed to obtain a microstructure composed of a Al-rich matrix (α-Al) with plate-like Si particles dispersed within interdendritic regions, composing a eutectic mixture with the Al_2Cu intermetallic phase formed by α-Al-eutectic + Si + Al_2Cu intermetallic + Fe intermetallic.

It is known that in high purity primary aluminum alloys, the iron content is relatively low, generally between 0.02

and 0.15 wt% [38, 43–49]. Another Fe-contamination source occurs in the preparation of primary Al–Si alloys, since commercially pure silicon can exhibit up to 0.6 wt% of Fe [41]. In Al–Si alloys, due to the presence of Fe, the formation of intermetallic Fe phases is inevitable. Basically iron-rich phases can be grouped into three kinds of morphologies: polyhedral or star-like, Chinese script and platelet [49], and the most observed among them is β-Al_5SiFe with platelet-like morphology, which occurs due to the reduction of the solubility limit of iron in aluminum, via solidification, and that depending on the Fe and Si contents is segregated into the interdendritic regions, composing the final microstructure of the eutectic mixture [40–45]. The presence of the β-Al_5FeSi phase has a considerable impact on mechanical properties. As this intermetallic phase presents needle-like platelet morphology, fragile characteristic and little interaction with the dendritic matrix, the mechanical properties of the Al–Si alloy are compromised [38–45]. The ultimate tensile strength and the ductility decrease in the presence of this intermetallic phase. It is concordant in the literature [38–48] that the main deleterious mechanism of the β phase to mechanical properties, is to block the eutectic liquid flow between the interdendritic regions during the solidification, forming porosities.

The literature [38–42] highlights several metallurgical processes as neutralizing the Fe-fragilizing effect, which alter the needle-platelet β-Al_5FeSi phase morphology to a Chinese script or polyhedral types morphologies, among which are the addition of alloying elements, high superheat of liquid metal and high growth and cooling rates. In the case of the addition of alloying elements, Mn is the most used to form the Chinese script type, however, Cu allows complex phase transformations via solidification, such as the peritectic reaction, characterized in Al–Si–Cu–Fe alloys by Liquid + β-Al_5FeSi → ω-Al_7Cu_2Fe which, depending on the V_L and C_R levels, can be observed in the platelet and blocky types morphologies.

It is known that studies on the microstructural evolution and correlation with tensile properties, via directional solidification, have been elaborated usually considering devices that promote upward growth. There are few investigations relating fracture feature to the solidification microstructural and thermal parameters of alloys solidified horizontally under transient conditions. In the sense, this work focuses on interrelations among growth rate (V_L), cooling rate (C_R), local solidification time (t_{SL}), secondary dendritic spacings ($λ_2$), morphologies of Si and IMCs,

microhardness (HV), yield strength ($σ_{YS}$), ultimate tensile strength ($σ_{UTS}$) and elongation (E%) of a horizontally solidified Al–7wt%Si–3wt%Cu–0.3wt%Fe alloy.

2 Experimental Procedures

The investigated AlSiCuFe alloy was elaborated from its high purity Al, Cu and Si elements (> 99.5%). The final chemical composition of the prepared alloy is shown in Table 1. It is emphasized that the presence of the iron element is as impurity originating mainly from the primary aluminum. The quantitative and qualitative chemical analyzes of investigated alloys were performed by Q4 TAS-MAN–CCD based optical emission spectrometer for metal analysis.

Figure 1 shows a schematic representation of the experimental set used in this work. The water-cooled horizontal solidification device (Fig. 1a) has been designed to promote the solidification in the horizontal direction from a stainless steel plate, located on one side of a rectangular ingot also in stainless steel. A stainless steel mold used was 150 mm long, 60 mm wide, 60 mm high and 3 mm thick and the thermal contact condition at the metal–mold interface was standardized with the heat-extracting surface being polished. Figure 1b shows an assembly scheme of the apparatus used to obtain the experimental solidification path for checking the liquidus and solidus temperatures of the investigated alloy as well as the inflection points in the experimental curve, which indicate the beginnings of the complex phase transformations. This has been used for comparison with the Scheil–Gulliver non-equilibrium solidification path calculated by Thermo-Calc software using database TTAL7 (ThermoTech Aluminum Thermal Database v.7).

A set of eight type K thermocouples were used in the metal considering the center line corresponding to the longitudinal axis and the experimental thermal records were applied to obtain the thermal parameters V_L, C_R and t_{SL}. A superheat of 10% above the liquidus temperature (T_L) of the investigated alloy was adopted for the beginning of the horizontal solidification experiments. The accuracy in the thermal parameters calculation was based on the reliability of the thermal data collected during the thermodynamic transformations developed in the transient directional solidification process assumed in this investigation. In this sense, the cooling curves generated by the thermocouples have allowed to obtain the results of the ordered pairs: positions × liquidus

Table 1 Chemical composition of the alloy investigated

Elements (wt%)										
Si	Fe	Cu	Mn	Mg	Cr	Ni	Zn	Ti	Be	Al
7.407	0.325	3.449	0.026	0.0027	0.012	0.016	0.199	0.023	0.00031	Bal.
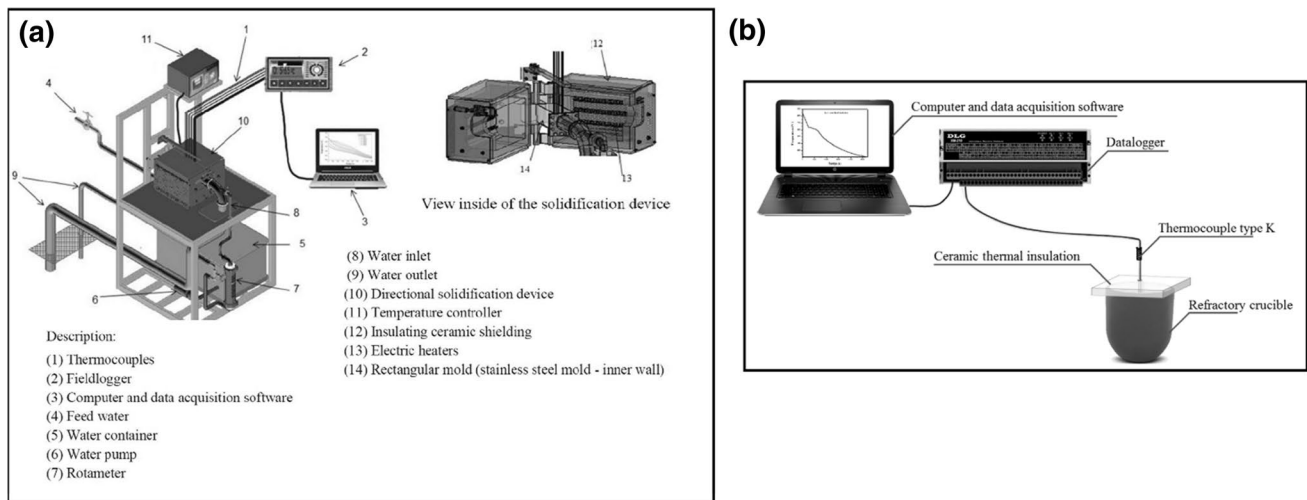
Fig. 1 Complete set of the solidification apparatus used in this work: **a** Water-cooled horizontal solidification device and **b** assembly of the apparatus to obtain the experimental solidification path

isotherm passage time (P, t), collected from the intersections of the line representing the T_L of the studied alloy with the respective curves. This has resulted in plotting a power function given by the general formula:

$$P = Constant(t)^n \qquad (1)$$

The experimental growth rates were determined by the derivative of the function

$$P = f(t) \qquad (2)$$

i.e.,

$$V_L = dP/dt \qquad (3)$$

The experimental cooling rates were obtained through the derivative of a second order polynomial curve, which was adjusted from a small experimental points range immediately before and after the experimental time of passage of the liquidus isotherm. As follows:

$$C_R = dT/dt \qquad (4)$$

Okamoto and Kishitake [37] have used only one point before and after the passage time of T_L. The cooling curves have also been used to determine the local solidification times (t_{SL}), which have been obtained by direct readings of the difference between the passage times of the solidus and liquidus isotherms by each thermocouple [7, 30].

Selected longitudinal (parallel to the growth direction) sections of the directionally solidified samples at 2, 4, 8, 10, 15, 20, 25, 30, 40, 50, 70, 80 and 100 mm from the metal/mold interface, were polished and etched with a solution of 5% of NaOH in water for micrograph examination. The dendritic microstructure was observed and characterized by the measurement of the secondary dendritic spacing. Figure 2 shows the cut-off scheme from the as-cast ingot of the

samples for metallographic examination and the methodology used for λ_2 measuring.

The mechanical properties evaluated in this work are Vickers microhardness and tensile properties including yield strength (σ_{YS}), ultimate tensile strength (σ_{UTS}) and elongation (E%). The mechanical tests were performed according to ASTM standards: E384/11 and E8 M/04. The adopted Vickers microhardness was the average of at least 20 measurements on each sample. The tensile tests were elaborated with a strain rate of 5×10^{-2} mm s^{-1} and in order to guarantee the reproducibility of the results, three samples were machined for each position. A schematic drawing of the cut-off of the specimens from the as-cast ingot is shown in Fig. 3a, b shows the geometry and dimensions of the specimen.

3 Results and Discussion

Figure 4a shows the solidification path of the Al–7wt%Si–3wt%Cu–0.3wt%Fe alloy predicted by Thermo-Calc software based on the Scheil–Gulliver model (no diffusion in solid phases, infinite diffusion in liquid, and thermodynamic equilibrium at the solid/liquid interface), i.e., the mass fraction of the phases versus temperature. In addition, experimental cooling curve and its respective first derivative (dT/dt, which indicates the instantaneous cooling rates) are presented in Fig. 4b in order to observe and confirm the complex phase transformations that occur during the solidification. It can be noted in Fig. 4a that the first formed phase consists of an aluminum-rich dendritic microstructure (α-Al) at *liquidus* temperature, followed by the formation of an eutectic
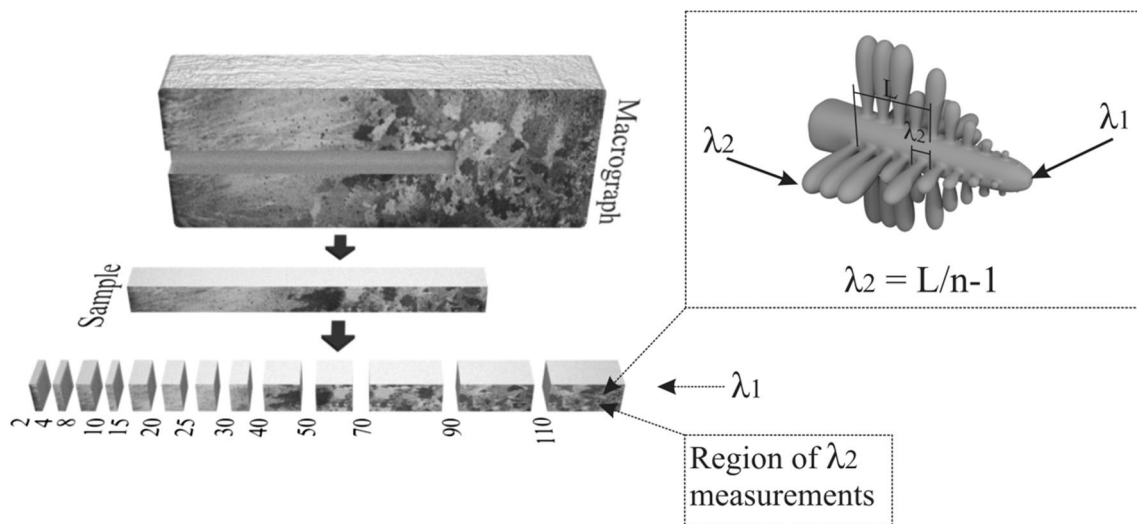
Fig. 2 Representative scheme of the methodology used for removal of samples from the ingot for metallographic examination and measurement technique of λ_2
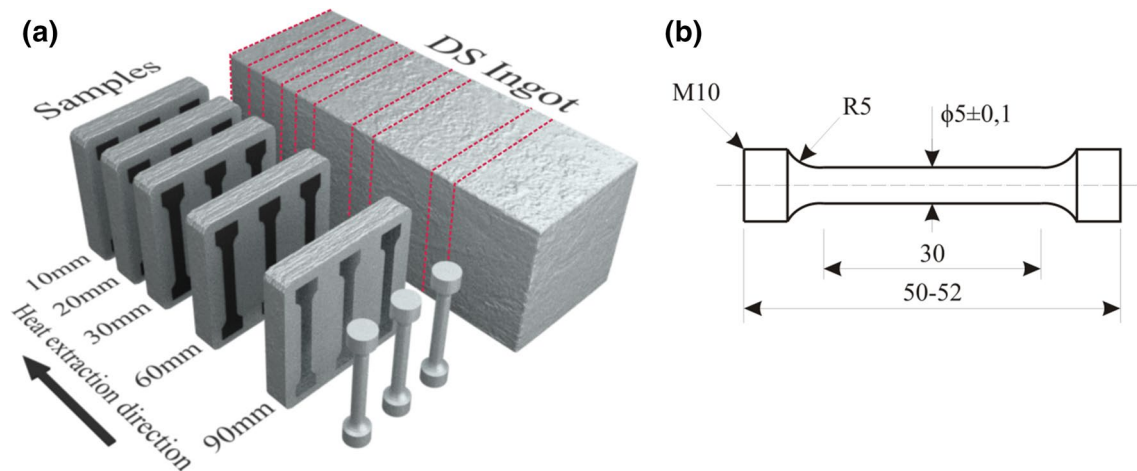

Fig. 3 Schematic representation of: **a** removal of the samples for the tensile test, and **b** geometries and dimensions of the samples according to ASTM standards: E384/1

[(α-Al)eutectic + Si particles] mixture, and at the end of the solidification (*solidus* temperature) the resulting microstructure is composed of a Al-rich dendritic primary phase (α-Al) and second segregated phases between interdendritic regions, composed of a eutectic intermetallic [(Al-α)eutectic + Si particles + Al$_7$Cu$_2$Fe(ω) + Al$_2$Cu(θ)] phases mixture. It should be noted that under non-equilibrium conditions and with low cooling rates the occurrence of iron intermetallic phase transformations, that is, the intermetallic Al$_5$SiFe (β) phase is transformed by peritectic reaction in the intermetallic Al$_7$Cu$_2$Fe (ω) phase, i.e., β + Liq. → ω. Furthermore, Fig. 4b shows the curve (T = f(t)) representing the experimental solidification path and its respective first derivative (dT/dt). It can be noted,

at the inflection points of the first derivative curve, the morphologies of the resulting microstructures of the investigated alloy.

Figure 5 presents the experimental curves obtained for the investigated alloy by the thermal analysis via horizontal solidification. Each experimental cooling curve refers to a thermocouple inserted into the horizontally solidified ingot at specific distance from the cooled interface considering the center line corresponding to the longitudinal axis. As can be seen, the slopes of the cooling curves were progressively steeper with decreasing distance from cooled interface. These curves have been used to calculate the solidification kinetics P = f(t) and the thermal parameters (V$_L$, C$_R$, and t$_{SL}$), and the results are shown in Fig. 6. It is emphasized that
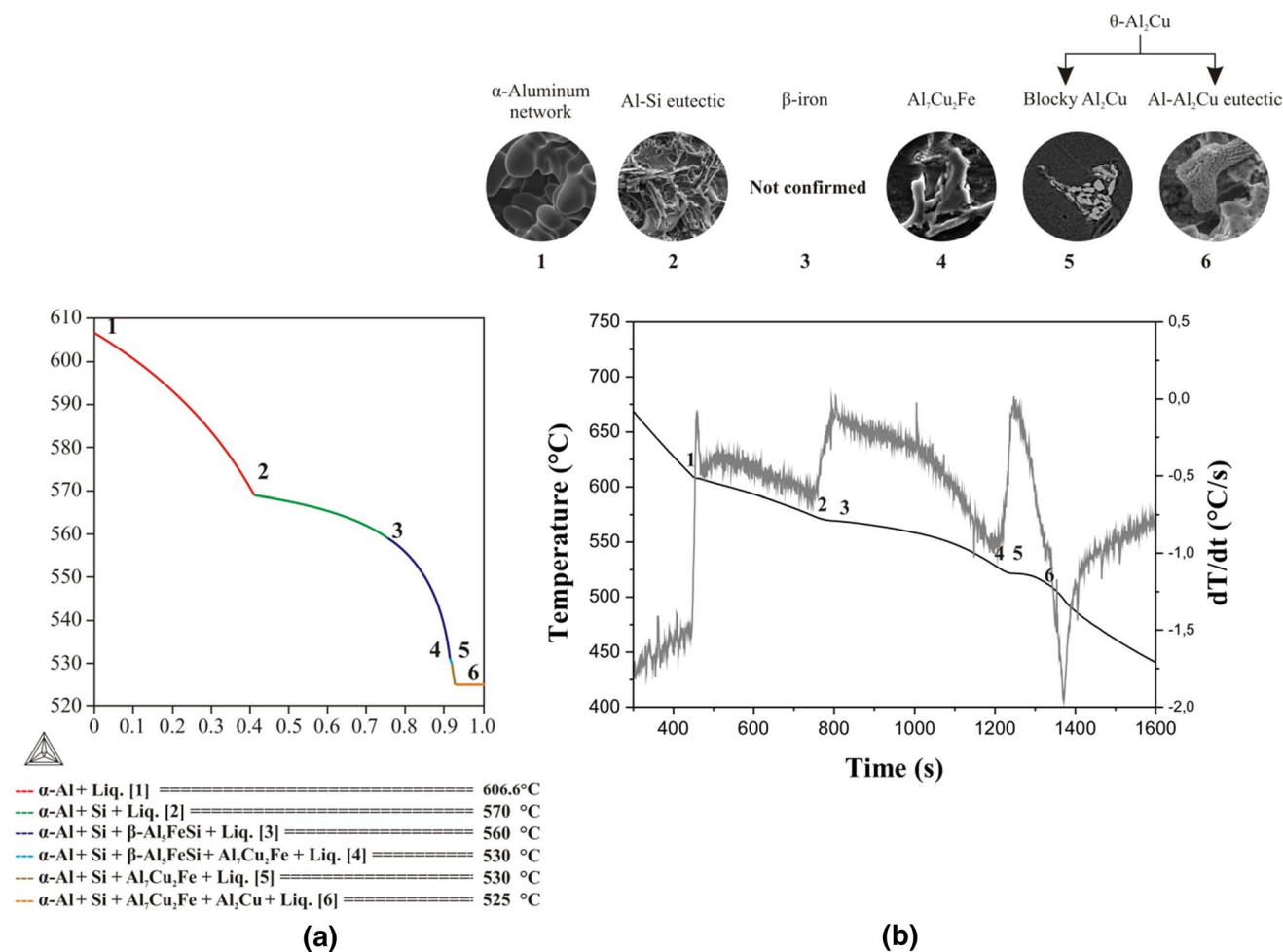
Fig. 4 Theoretical and experimental solidification paths for the investigated alloy obtained: **a** by Thermo-Calc, **b** experimentally and the first derivative of the experimental cooling curve
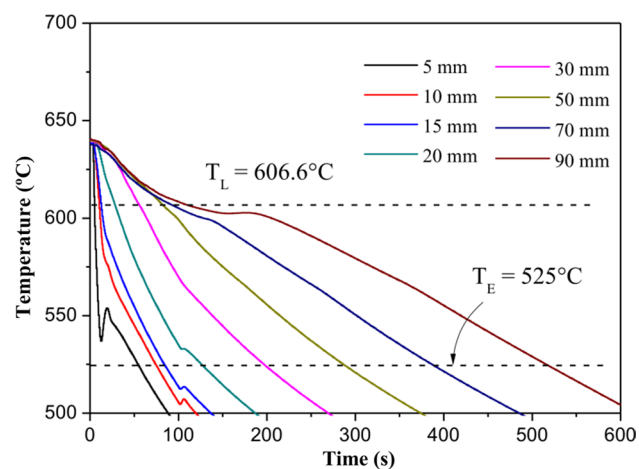
Fig. 5 Experimental cooling curves for the eight thermocouples obtained in the thermal data acquisition during horizontal solidification. T_L and T_E are the liquidus and eutectic temperatures, respectively

the results of the thermal analysis, for the investigated alloy, have been recently published in our paper [46], which were used in this work to investigate the HV and tensile properties dependence on V_L, C_R and λ_2.

The typical solidification macrostructure and the corresponding microstructures for three positions from the cooled interface (metal/mold interface) are shown in Fig. 7. As the solidification progresses (Fig. 6a), a solid layer is formed from the metal/mold interface and grows as the solidification advances, which act as resistance to heat extraction. This has resulted in a decreasing profile of the growth and cooling rates (V_L and C_R, respectively), as shown in Fig. 6b. An Al-rich primary phase (α-Al) of dendritic morphology characterizes the microstructures along the horizontally solidified casting. Owing to higher C_R values, typical of areas that are near to the cooled surface (e.g., P = 10 mm), more refined microstructures may be seen, which become progressively coarser towards the casting interior (e.g., P = 90 mm). It can be observed in the dendritic microstructures presented
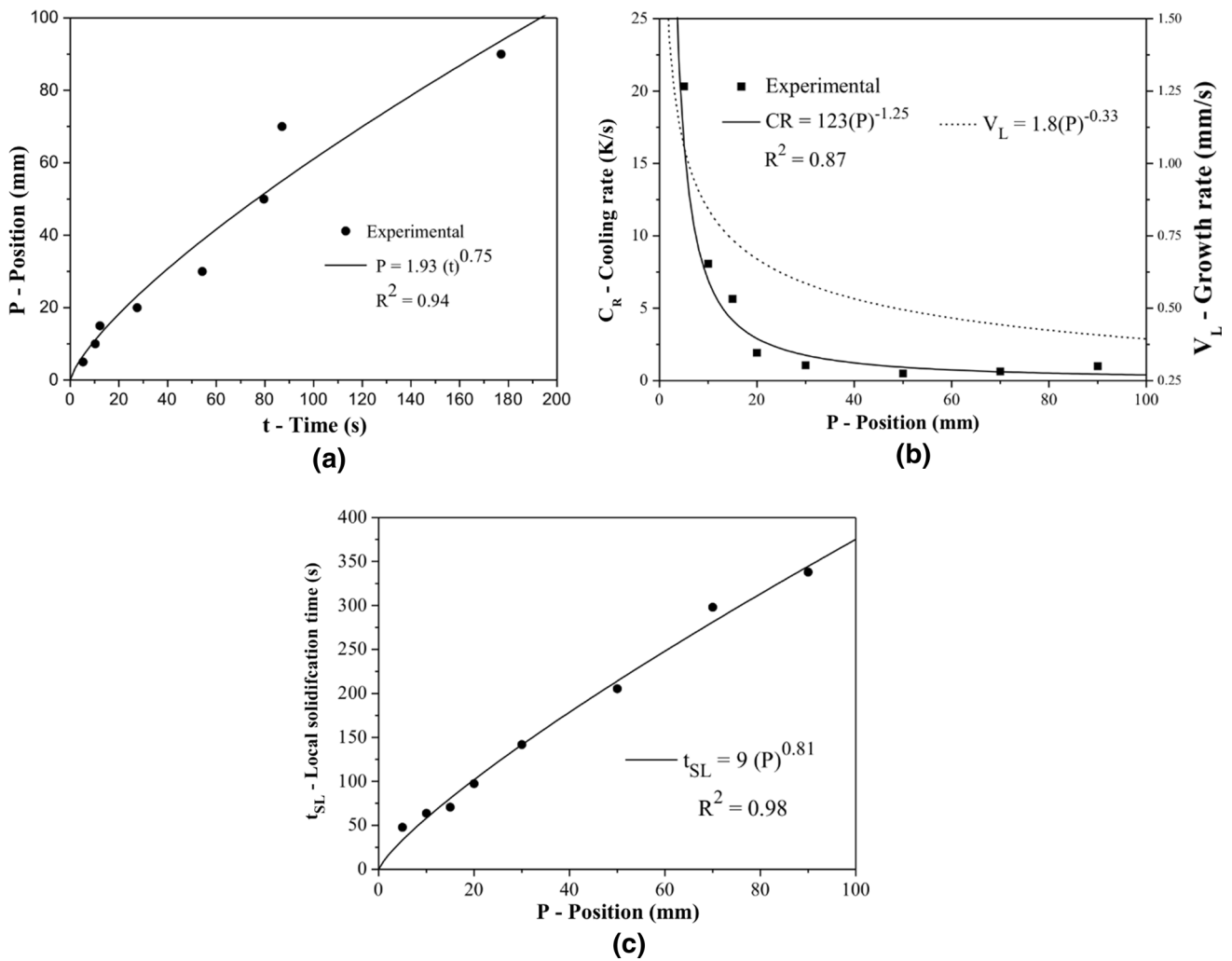
Fig. 6 Experimental results of: **a** solidification kinetics and **b** growth and cooling rates and **c** local solidification time

in Fig. 7 that the λ_2 values are equal to 24.18, 49.65 and 68.88 μm for positions equal to 10, 50 and 90 mm from the cooled interface, respectively.

The experimental results of the correlation between the secondary dendrite arm spacings with V_L, C_R and t_{SL} are shown in Fig. 8. It is observed for the studied alloy that, despite turbulent flows associated with melt convection during horizontal solidification, the mathematical expressions given by $\lambda_2 = 26(V_L)^{-2/3}$, $\lambda_2 = 50.6(C_R)^{-1/3}$ and $\lambda_2 = 8.1(t_{SL})^{1/3}$ characterize the growth laws of λ_2 as a function of V_L, C_R and t_{SL}, respectively, at the center line corresponding to the longitudinal axis of ingot. As previously mentioned, the use of indexes equal to $-2/3$, $-1/3$ and 1/3 in the experimental laws has been confirmed to satisfactorily represent λ_2 evolution with V_L, C_R and, t_{SL}, respectively, for binary alloys [4, 5, 15–18, 20–27, 33] and for ternary Al-based alloys [6–10, 12–14, 32–37] solidified under transient conditions. Moreover, it should be noted that

the experimental exponents values, obtained in the relation of $\lambda_2 = f(V_L$ and $t_{SL})$, that is, $-2/3$ and 1/3, are equal to the theoretical values proposed by the mathematical equations of the BK′ and RB′ models, respectively. The mathematic expressions referring to the RB′ model are represented by Eqs. 5 and 6. In this work, a theoretical and experimental study on λ_2 values has been performed. It can be seen in Fig. 9.

$$\lambda_2(RB) = 5.5\left(Mt_{SL}\right)^{\frac{1}{3}} \tag{5}$$

$$M(RB) = \cfrac{-\Gamma}{\sum_{j=1}^{n} m_j\left(1-k_j\right)\left(c_{fj}-c_{0j}\right)/D_j} \\ \ln\left(\cfrac{\sum_{j=1}^{n} m_j\left(1-k_j\right)c_{fj}/D_j}{\sum_{j=1}^{n} m_j\left(1-k_j\right)c_{0j}/D_j}\right) \tag{6}$$

Fig. 7 Typical solidification structures at macrostructural and microstructural scales resulting from horizontal solidification
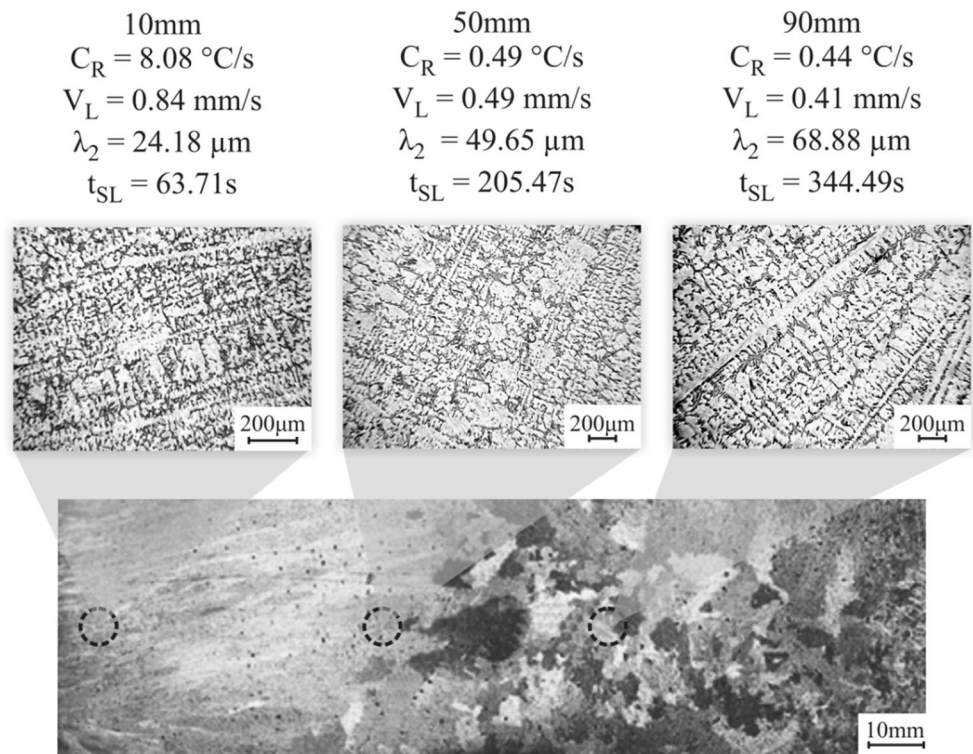
where Γ is the Gibbs–Thomson coefficient, c_0 is the alloy composition, m is the liquidus slope, c_f is the eutectic composition, D is the diffusion coefficient in the liquid, and k is the redistribution coefficient. The subscript "j" represents each alloying element and the sum encompasses all the solute elements of the multicomponent alloy.

Table 2 presents the thermophysical properties of the investigated alloy that were calculated by a numerical model, developed by Nascimento et al. [50], which connects in real run time execution to Thermo-Calc and its database TTAL7 (Thermo Tech Aluminum Thermal Database).

It is noted by Fig. 9 that the theoretical values overestimate the experimental results and the ratio between experimental and theoretical secondary dendrite arm spacings is equal to 0.54, i.e., λ_2(Experimental)/λ_2(RB) = 0.54. Thus, it is suggested that the mathematical expression of the RB′ model [Eq. (5)] has to be corrected by a factor K, that is, λ_2(RB) = (K).5.5 $(MtSL)^{1/3}$ (where K = 0.54). Araújo et al. [7] have found a factor equal to 0.56 for horizontally solidified Al–5.5wt%Si–3wt%Cu alloy. The equations obtained by the authors were: λ_2(Experimental) = 7.8$(t_{SL})^{1/3}$ and λ_2(RB) = 13.9$(t_{SL})^{1/3}$.

SEM micrographs, as well as the area mapping and pointwise EDS microanalysis can be seen in Fig. 10 for P = 2 mm and P = 90 mm from the cooled interface of the horizontally solidified ingot (positions associated with high and low C_R values, respectively). It can be seen Si particles/IMCs/eutectic mixture distributed in the interdendritic regions, and finer

Si particles, Fe-rich and Al_2Cu intermetallic phases observed for P = 2 mm (position near to the cooled surface). A key difference observed for position with the highest C_R values is an overall refinement of the entire microstructure. Like for the scale of Al-rich matrix, faster cooling limits the growth of secondary phases and, as consequence, finer particles will be found in smaller interdendritic regions. Among the observed phases, it is highlighted the θ-Al_2Cu intermetallic compound in the finer eutectic-like form, and the morphology of this phase in the blocky type was only possible to see in the fracture surfaces. In Al–Si alloys the most common Fe intermetallic phase observed is the β-AlFeSi phase [35–38], which has a deleterious influence on the mechanical properties of these alloys, especially the ductility and castability [35]. On the other hand, multicomponent Al–Si based alloys with Cu and/or Mg addition inhibit the formation of the β phase, changing it to other forms, such as ω-Al_2Cu_7Fe phase, which has been observed in the final microstructure of the Al–7wt%Si–3wt%Cu–0.3.wt%Fe alloy investigated in this work.

The microhardness as well as the tensile mechanical properties have been analyzed in this work and the results are presented in Fig. 11. As can be seen, the σ_{UTS} and E% values of the ternary alloys examined in the present study were significantly affected by the magnitude of λ_2. It is observed higher σ_{UTS} and E% values for more refined dendritic microstructures, i.e., the effect of the higher growth and cooling rates (V_L and C_R) resulted in lower λ_2 values
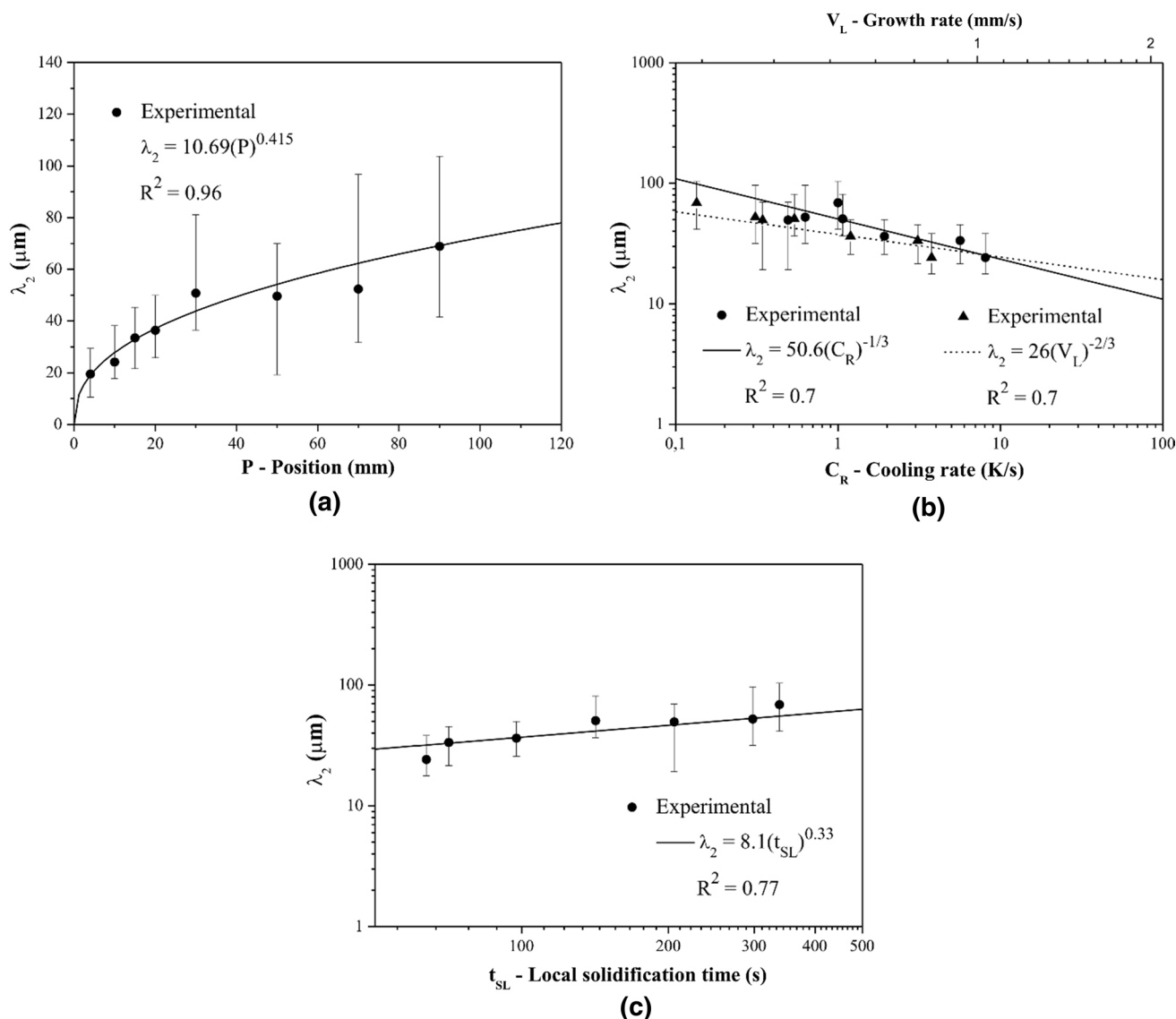
Fig. 8 Dependence of the secondary dendrite arm spacing as a function of: **a** liquidus isotherm position, **b** growth and cooling rates, and **c** solidification local time

and, as consequence, it has increased the ultimate tensile strength and elongation. The application of Hall–Petch type equations seems to be appropriate to characterize the variation of both σ_{UTS} and E% with λ_2. In general, it is expected that a more homogeneous distribution of Si particles/IMCs/eutectic mixture, which occurs for lower λ_2 values (specimens associated with fast solidification), favors the increment in ultimate tensile strength. On the other hand, the HV and σ_{YS} properties have not been affected, i.e., both remain constant along the as-cast ingot.

It is important to emphasize that there are still gaps in the literature on the combined effects of thermal parameters and the distribution, size and morphology of Si particles with IMCs contained in the eutectic mixture of Al–Si-(with

addition of Cu or Mg) alloys on the mechanical properties. It is very well established that ultimate tensile strength (UTS) increases with increasing C_R and with decreasing λ_2, while results on yield strength (YS) and microhardness (HV) are controversial [50–55]. Most of the results presented by these studies show that the yield stress is not affected by the microstructural arrangement. Figure 12 presents a comparison with the literature [7, 22, 29, 30, 55].

For results of HV = f(λ_2), It was observed that similar and contrary HV behavior have been reported by Costa et al. [30] and Araújo et al. [7] during upward and horizontal directional solidification of the Al–5.5wt%Si–3wt%Cu alloy, respectively, i.e., relative to the work of Ref. [30] the authors found a constant HV value equal to 76 kg/mm^2
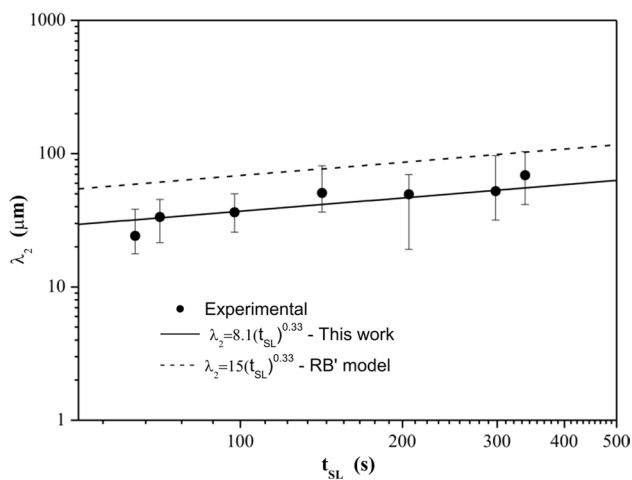
Fig. 9 Comparison between λ_2 values calculated by this work and by the RB′ model

Table 2 Thermophysical properties of the investigated alloys applied in the RB′ model, for the calculation of the theoretical values of λ_2

Properties	Symbol	Units	Value
Liquidus temperature	T_L	°C	606.6
Solidus temperature	T_S	°C	525
Liquidus slope	M	°C $(\%)^{-1}$	3.71 (Cu) 6.93 (Si)
Partition coefficient	K	–	0.143 (Cu) 0.119 (Si)
Solute liquid diffusivity	D_L	$m^2\,s^{-1}$	3.98×10^{-9} (Cu) 2.21×10^{-9} (Si)
Gibbs–Thomson coefficient	Γ	m K	7.89×10^{-7}
Alloy composition	C_0	(wt%)	3.0 (Cu) 7.0 (Si)
Final liquid composition (often assumed to be the eutectic composition)	C_f	(wt%)	26.9 (Cu) 11.6 (Si)

along the length of the as-solidified ingot, on the other hand, Araújo et al. [7] have characterized a HV dependence on λ_2 given by the mathematical equation $HV = 167(\lambda_2)^{-0.17}$, as observed in Fig. 12a. Costa et al. [30] and Araújo et al. [7] proposed a correlation of $\lambda_2 = f(C_R)$ given by $\lambda_2 = 41(C_R)^{-1/3}$ and $\lambda_2 = 37(C_R)^{-1/3}$, respectively, thus, considering the same levels of C_R, it is observed that lower λ_2 values are predicted in the results of Araújo et al. [7], which explains the higher HV values.

Figure 12a also presents comparative results with the Al–3wt% Cu alloy [7, 22, 55] solidified in both growth directions (upward and horizontal), by which, due to the presence of hardening phases (Si/IMCs) in the interdendritic regions, higher HV values are observed for Al–X.wt%Si–3wt%Cu

alloys (X = 5.5 and 7). Vasconcelos et al. [31] have carried out an experimental study with horizontally solidified Al–6wt%Cu and Al–6wt%Cu–8wt%Si alloys and the results, for both investigated alloys, show that HV increases with the decrease of the primary dendritic spacings (λ_1) and higher HV values were observed for the ternary alloy. As previously reported, Brito et al. [28] found results completely contrary to those shown in Fig. 12a for Al–Mg and Al–Si–Mg alloys, that is, HV increased with the increase of λ_2.

With regard to the tensile properties, for the ultimate tensile strength, elongation (E%) and yield strength similar trends were found by Samuel and Samuel [50] and Samuel et al. [51] in Al–Si–Cu alloys (319), that is, the σ_{UTS} and E% values became higher for lower λ_2 values, while the yield strength is practically unaffected. Goulart et al. [53] investigated the influence of thermal parameters on the as-cast microstructure of hypoeutectic Al–X.wt%Si alloys (X = 5 and 9), and they reported that the ultimate tensile strength increases with increasing solute content and with decreasing of λ_2, on the other hand, the yield strength has shown to be independent of both alloy composition and dendritic arrangement. In contrast on heat treated AA319-type alloys (containing Sr, Fe and P element additions), Li et al. [52] have reported that, σ_{UTS}, σ_{YS} and %E decrease with the decrease of C_R, i.e., increase of λ_2, in both T5/T6-heat treatment conditions.

Reyes et al. [54] developed directional solidification studies with hypereutectic Al-XSi alloys (X = 15 and 18 wt%), assuming two melt superheats ($\Delta T = 6\%$ and 23%), and the results showed that σ_{UTS} decreased with the interphase spacing (λ) for $\Delta T = 6\%$, but it was not affected by λ for the highest ΔT (23%) value. Franco et al. [56] also proposed for Al–10wt%Si–Xwt%Cu alloys (X = 2 and 5) a relation of $\sigma_{UTS} = f$(primary dendrite arm spacing–λ_1) through Hall–Petch mathematical expressions, reporting a similar trend of σ_{UTS} with λ_1, that is, UTS increases with the decrease of λ_1.

Figure 12b shows a comparative analysis with the literature [29, 55] for $\sigma_{UTS} = f(\lambda_2)$. This is observed a good agreement between the results of this work and that of Çadirli [55], and Chen et al. [29] have found higher σ_{UTS} values for the Al–7wt% Si alloy with addition of Mg.

An overview of fracture surfaces and SEM images with EDS mapping are shown in Figs. 13 and 14, respectively, for three as-solidified samples along the length of the ingot. It is clearly evidenced in Fig. 13 the presence of void defects (pores) in columnar dendrites, increasing in size at the positions of fractured samples equal to 20 and 90 mm, that is, for lower V_L and C_R values and higher λ_2 values. This may be due to the formation of porosities due to the solidification contraction and presence of gases, but may also occur due to the nucleation of intermetallics Fe phases, mainly the β-Al_5FeSi phase during solidification at high temperatures. It is known that there is agreement in the literature [38–46]
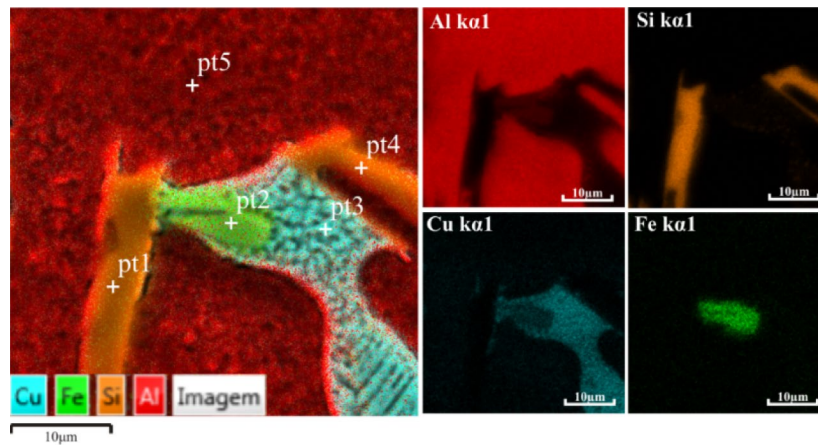
P = 30mm					
Point	Weight (wt.%)				Phase
	Al	Si	Cu	Fe	
1	7.12	91.98	0.74	0.16	Si particle
2	50.94	9.02	18.11	21.92	$Al_2Cu_7Fe(\omega)$
3	26.76	12.18	60.92	0.13	$Al_2Cu(\theta)$
4	56.69	41.73	1.58	-	Si particle
5	96.11	1.05	2.84	-	α-Al Dendritic

(a)
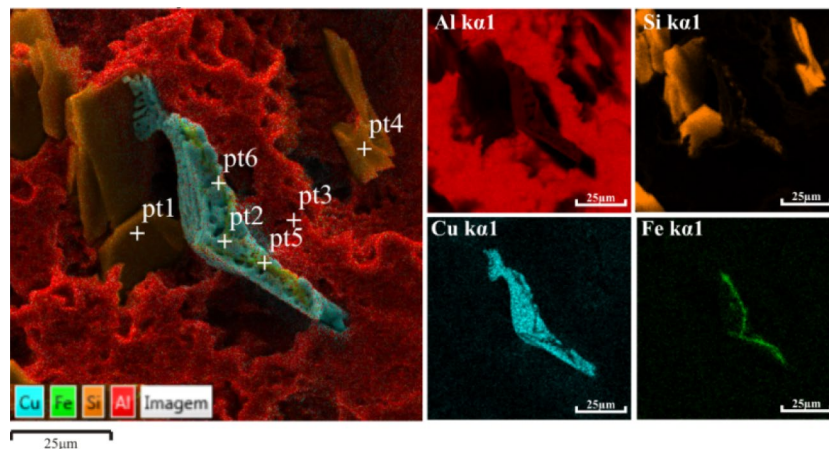
P = 90mm					
Point	Weight (wt.%)				Phase
	Al	Si	Cu	Fe	
1	12.62	85.12	2.21	0.04	Si particle
2	49.77	14.57	32.01	3.64	$Al_2Cu(\theta)$
3	95.51	1.45	3.05	-	α-Al Dendritic
4	3.61	95.66	0.66	0.07	Si particle
5	40.57	34.97	9.72	14.73	$Al_2Cu_7Fe(\omega)$
6	48.36	23.1	18.08	10.46	$Al_2Cu_7Fe(\omega)$

(b)

Fig. 10 SEM mapping and EDS composition obtained for two positions in the ingot from the cooled base: **a** P = 30 mm, V_L = 0.59 mm/s, C_R = 1.75 K/s e λ_2 = 50.80 μm, and **b** P = 90 mm, V_L = 0.41, C_R = 0.44 K/s e λ_2 = 68.88 μm
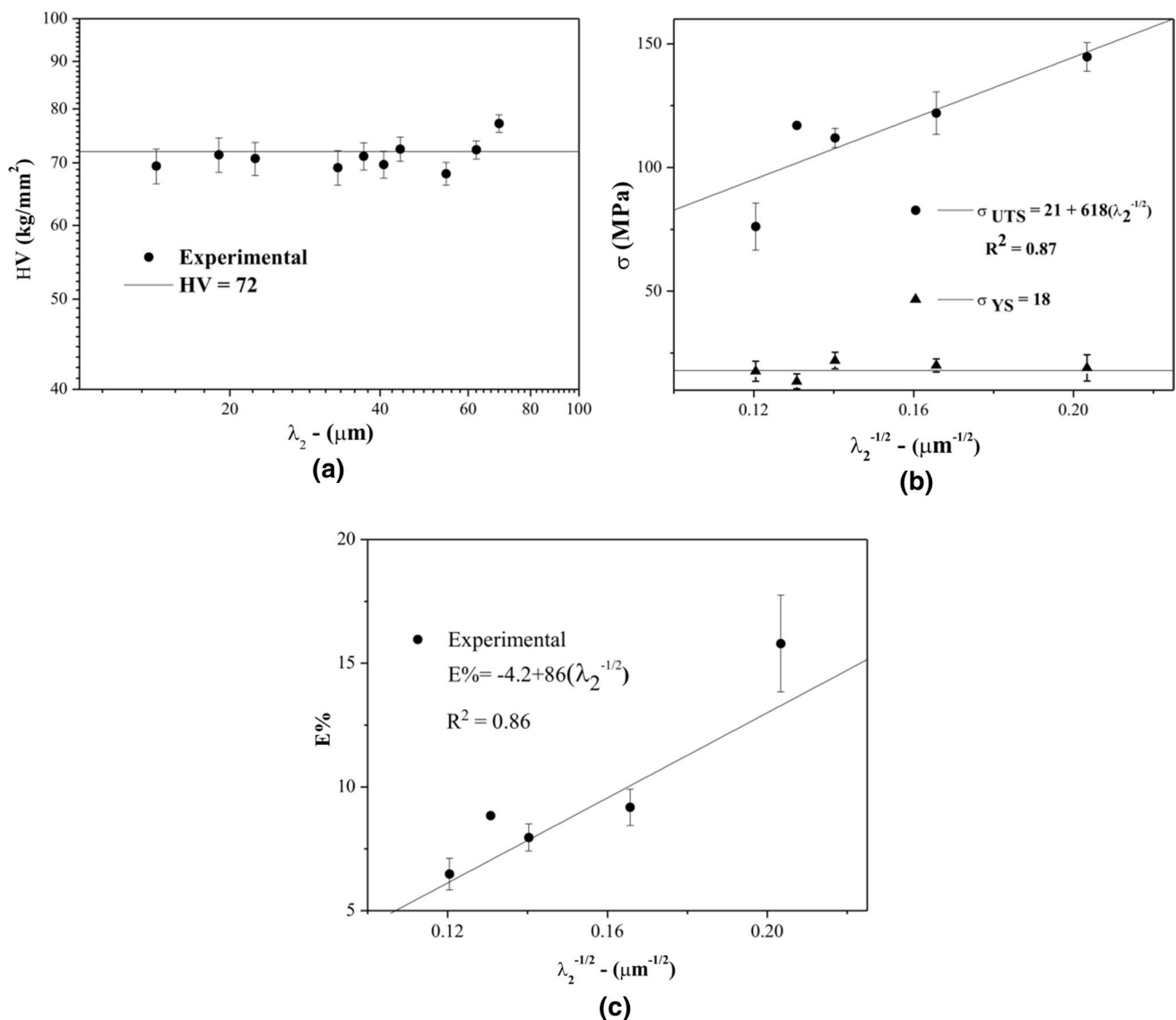
Fig. 11 Experimental results of the dependence of the investigated mechanical properties as a function of λ_2: **a** microhardness-HV, **b** yield strength and ultimate tensile strength-σ_{YS} and σ_{UTS}, respectively, and **c** elongation-E%

that the β phase is a facilitator in the formation of voids due to lack of liquid feed in the interdendritic channels. The β phase and the following formed with the continuity of the cooling (ω-Al$_2$Cu$_7$Fe phase), via solidification of the investigated alloy in this work, at the time reaching the temperatures of 560 °C and 530 °C (see Fig. 4), respectively, are blocking the interdendritic regions and, as a consequence, obstructing the flow of eutectic liquid between these regions.

According to Malgozarta [47], the matrix of AlSiCu alloys (Fe as impurity), constituted by the dendritic (α-Al) phase, is soft plastic and exhibits ductile or dimple fracture mode by the activation of the slip system mechanism. Dimples are cuplike depressions that forming by a process known as microvoid coalescence and occur by the nucleation of small

discontinuities (voids) usually on the interface between hard dispersed intermetallic phases, micropores, microcracks or inclusions [47, 48]. On the other hand, cleavage is a low-energy fracture that propagates along well-defined low-index crystallographic planes known as cleavage planes and they are characteristic for local crystallographic orientation, in the case of the ideal cleavage fracture, they are smooth in the atomic scale [47, 48]. It is highlighted that (α-Al)-matrix crystalizes in the form of non-faceted dendrite with metallic bond and, in contrast, the hard brittle Si particles present in this alloys are almost pure and faceted crystals with covalent bond [45, 46]. These crystals have a rather cleavage fracture mode.

In Fig. 14, irregular cleavage planes are shown for all cases, and more extensive for positions farther from the
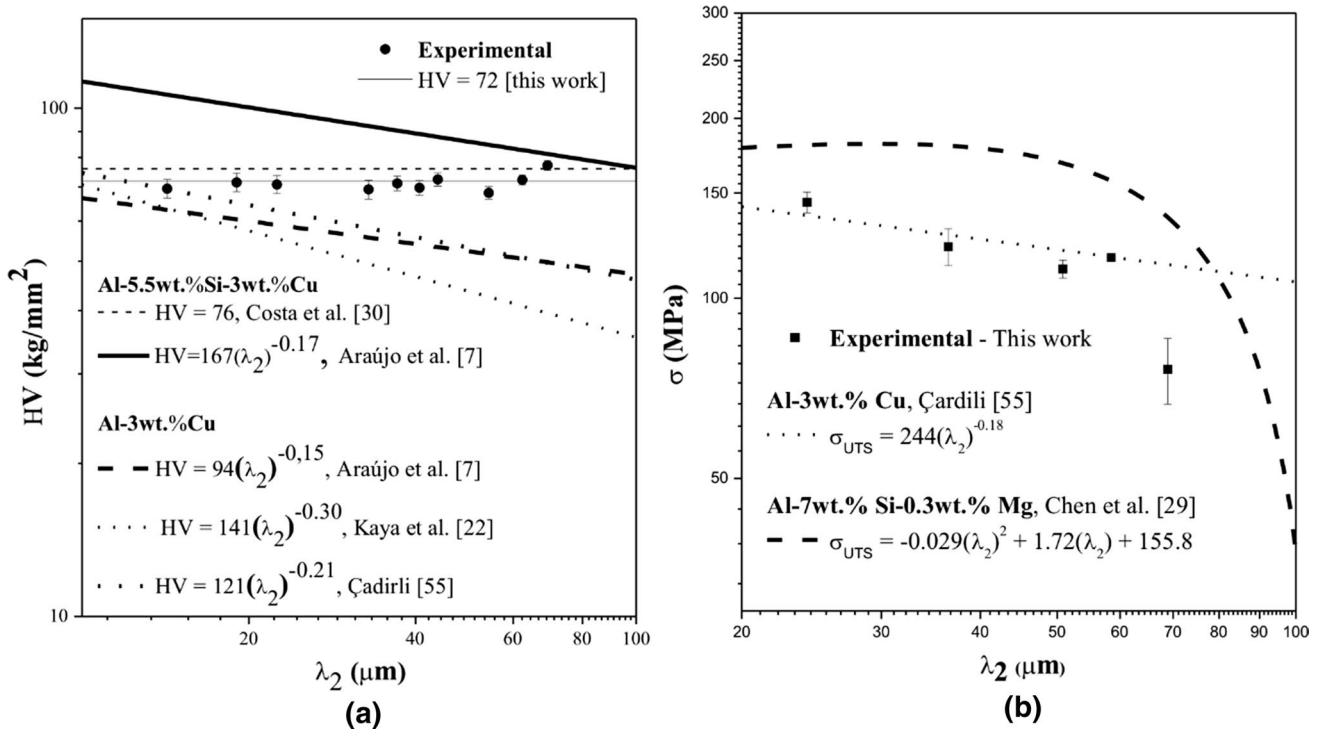
Fig. 12 Comparison with the literature on Hv and σ_{UTS} results: **a** Hv = f(λ_2) and **b** σ_{UTS} = f(λ_2)
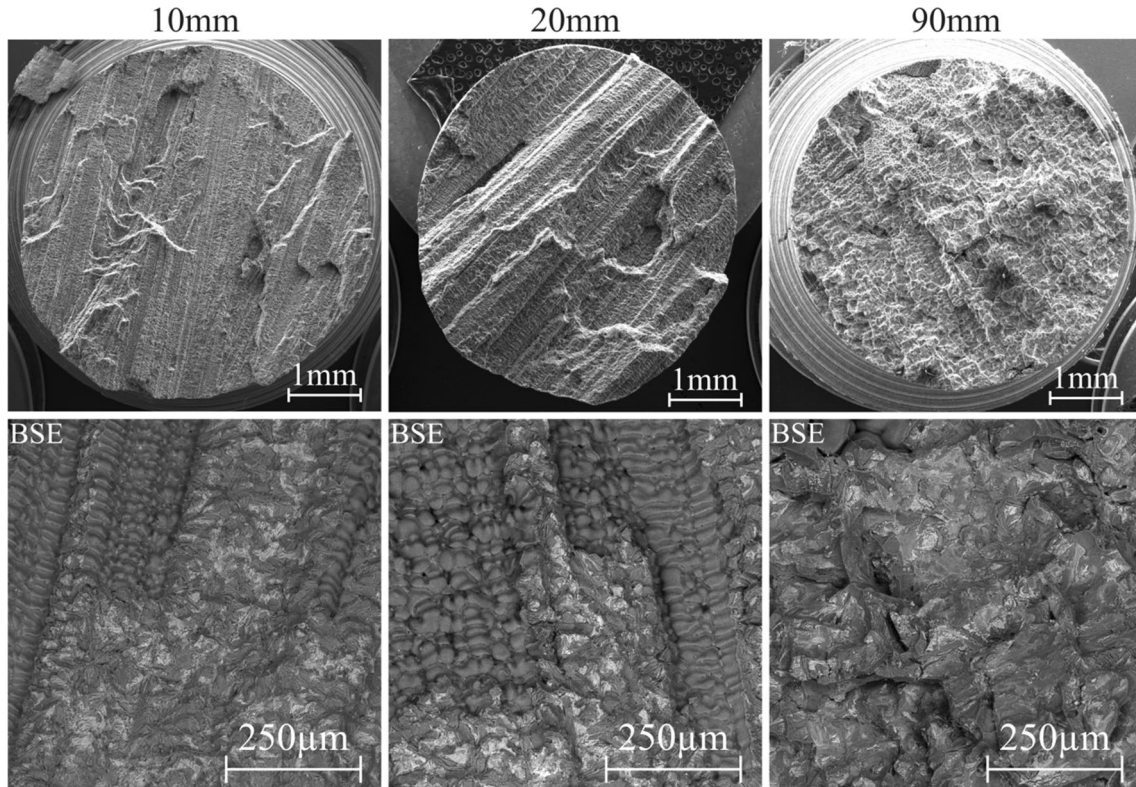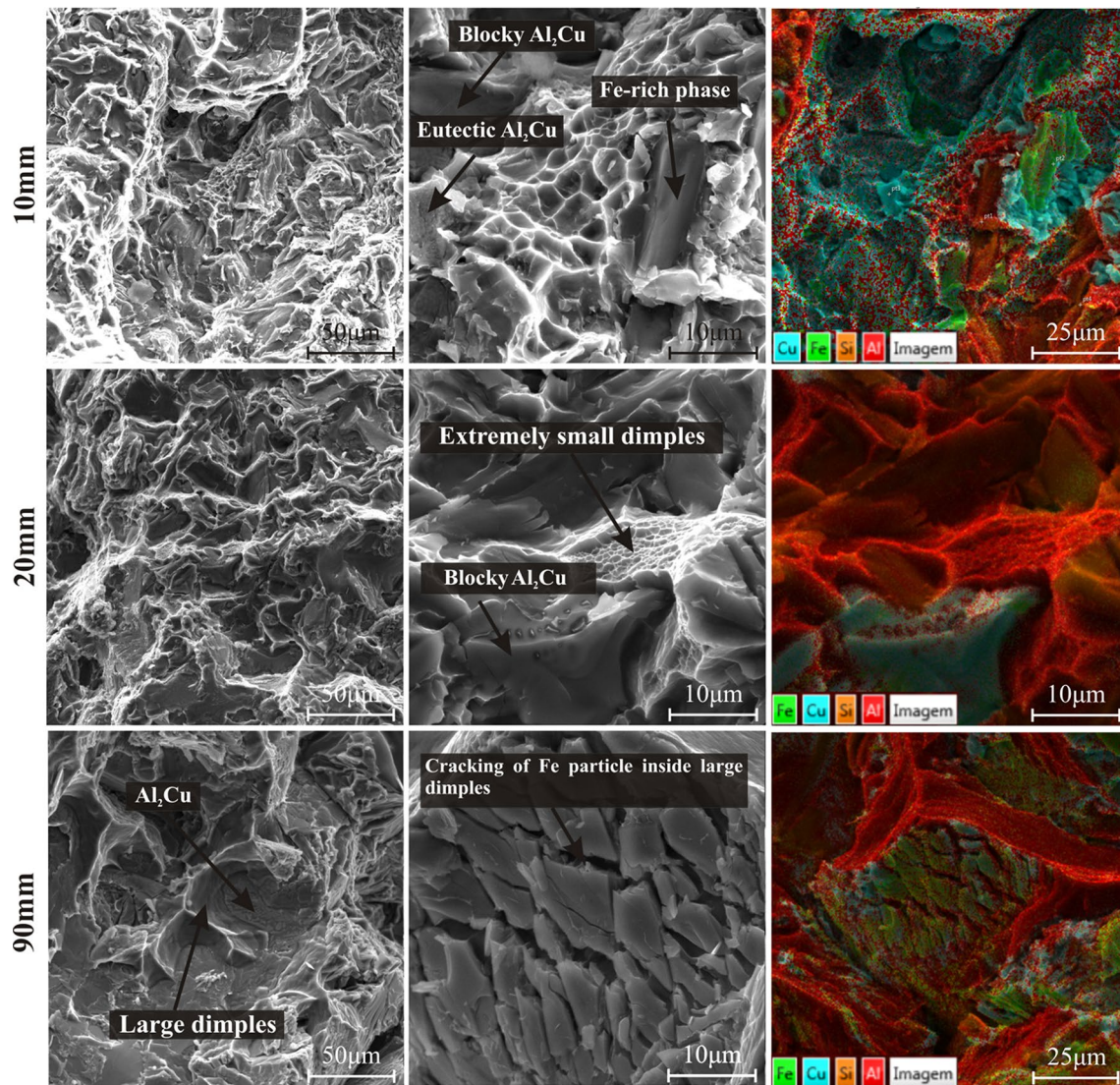

Fig. 13 Overview fracture surface of samples of the horizontally solidified alloy, submitted to the tensile tests

Fig. 14 SEM fractographs and EDS mapping of tensile sample of the investigated alloy

cooled interface, with some rip grooves accompanied by dimples, typical quasi-cleavage fracture mode. For higher V_L and C_R values the dendritic microstructure is more refined and, as consequence, decreases: the number and size of the cast defects; the sizes of Si particles (with morphological changes from lamellar to fibrous or spheroidal) and the sizes of Al_2Cu and Fe intermetallic phases. In addition, it is noted that for smaller λ_2 values the area and size of the cleavage planes decrease, on the other hand, the number of dimples increases and the surface of the fracture is covered by fine and equiaxed dimples, typical characteristic of ductile fracture, resulting in higher σ_{UTS} and E% values (Fig. 11b, c). This has allowed noting the existence of a transition from ductile to fragile fracture with the advance of horizontal solidification.

Figure 15 shows the fracture profile for two positions in the ingot of fractured samples, with smaller and larger λ_2 values (10 mm and 90 mm, respectively). It is observed for both samples that the main crack profile line clearly shows the morphological feature of the Al-rich dendritic primary phase (α-Al). It can be seen from the EDS mapping of fracture profiles that the cleavage line is more prominent in the position equal to 90 mm, further away from the cooled interface, in which the secondary dendrite arm spacings are larger and from which nuclei of coarser hard particles, such as Si, θ-Al_2Cu and ω-Al_7Cu_2Fe. It is obvious to the fragmentation of ω-Al_7Cu_2Fe particles, with larger sizes, for the low cooling rate ($\lambda_2 = 68.88$ µm). In addition, porosities of larger sizes have been observed at P = 90 mm (see Fig. 12), which play an essential role in the crack process.
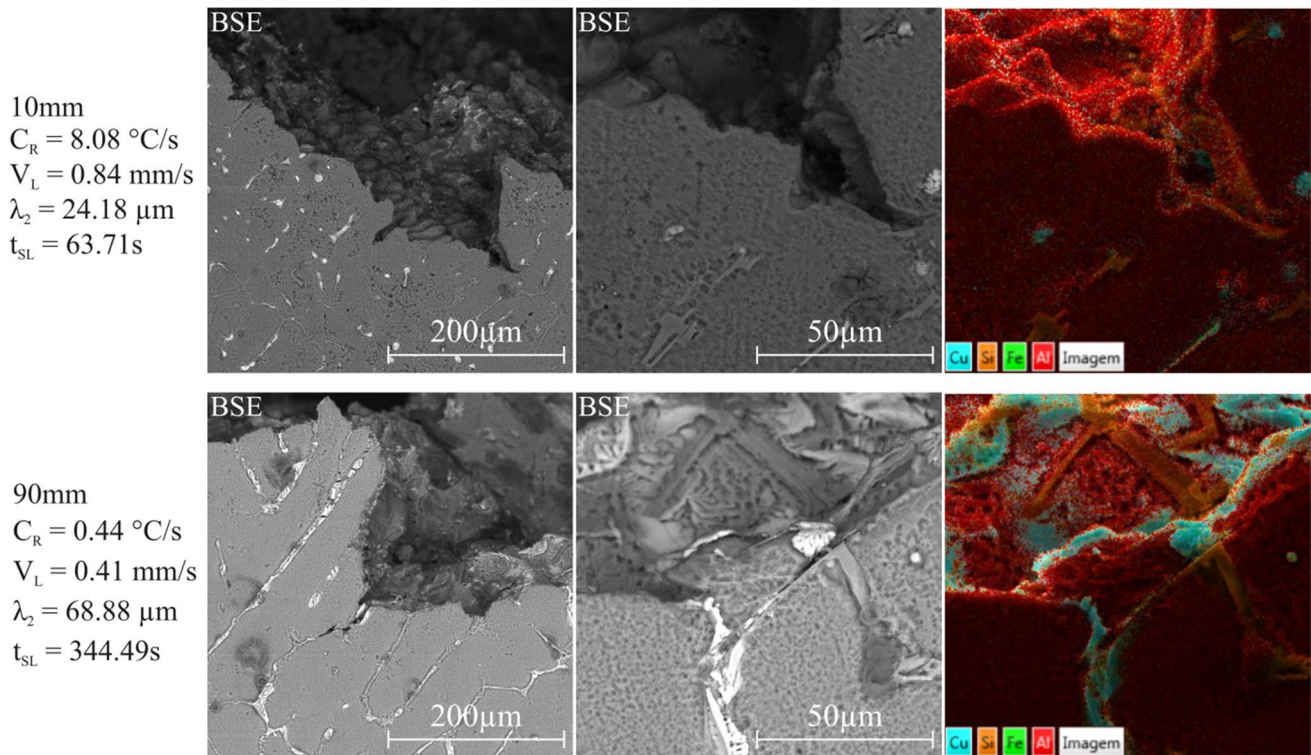
Fig. 15 General fracture profile with SEM mapping for two positions in the ingot of the investigated alloy

4 Conclusions

In view to the importance of multicomponent aluminum alloys for the automotive and aerospace industries, as the investigated alloy in this work, and considering the results obtained from this investigation, the following conclusions were drawn:

1. For the multicomponent AlSiCuFe alloy investigated in this work, the dependence of the secondary dendrite arm spacing as a function of the thermal parameters has been characterized by experimental growth laws given by the following general expression: $\lambda_2 = $ Constant.(V_L, C_R e t_{SL})^n, where n is equal to $-2/3$, $-1/3$ and $1/3$ to λ_2 varying with V_L, C_R and t_{SL}, respectively.
2. Although the growth law index of λ_2 as a function of t_{SL} determined by the RB′ model (Eqs. 5 and 6) was absolutely equal to that obtained experimentally, i.e., $\lambda_2 = $ Constant·$(t_{SL})^{1/3}$, the Constants values equal to 15 and 8.1, respectively, show that the theoretical λ_2 values overestimate the experimental values by approximately 85%.
3. In concomitant analysis of the phase transformations evidenced by the theoretical and experimental solidification paths with the SEM micrographs and EDS mapping and composition, it can be concluded that the final microstructure of the investigated AlSiCuFe alloy is composed of (α-Al) dendritic + (α-Ál)$_{eutectic}$ + Si particles + intermetallic ω-Al$_2$CuFe and θ-Al$_2$Cu particles. The β-Al$_7$FeSi phase has not been observed.
4. It was observed that the microhardness and the yield strength were not affected by the variations of the resulting microstructure from the horizontal solidification, giving values equal to 70 kg/mm^2 and 20 MPa, respectively. In contrast, it was found that the ultimate tensile strength and elongation were affected by the variation of the microstructure along the horizontally solidified ingot, i.e., higher σ_{UTS} and E% values were observed for lower λ_2 values. The dependence of σ_{UTS} and E% on λ_2 has been characterized by the following mathematical expressions: $\sigma_{UTS} = 21 + 618(\lambda_2)^{-1/2}$ and E% $= -4.2 + 86(\lambda_2)^{-1/2}$, respectively.
5. For the multicomponent investigated alloy, the fracture surfaces characterized by SEM and EDS mapping micrographs have shown less extensive cleavage planes accompanied by small dimples in fractured samples with lower λ_2 values. It has been observed that both cleavage planes and dimples increase in extension and size, respectively, with the gradual increase of λ_2. This has allowed to verify a transition from ductile to brittle fracture with the gradual reduction of the solidification thermal parameters (V_L and C_R).

References

1. I.J. Polmear, in *Light Alloys: From Traditional Alloys to Nanocrystals*, 4th edn. (Elsevier Butterworth-Heinemann, Amsterdam, 2006)
2. B. Altshuller, P.B. Dickerson, R.L. Heflin, in *Aluminum Brazing Handbook*, 4th edn. (The Aluminum Association Inc, Washington, 1990)
3. A.H. Musfirah, A.G. Jaharah, J. Appl. Sci. Res. **8**, 4865–4875 (2012)
4. D.L. Soares, A.S. Barros, M. Dias, A.L. Moreira, J.C. Filho, A.P. Silva, O.L. Rocha, Int. J. Electrochem. Sci. **12**, 413–428 (2017)
5. W.R. Osório, C.A. Siqueira, C.A. Santos, A. Garcia, Int. J. Electrochem. Sci. **6**, 6275–6289 (2011)
6. W.R. Osório, D.J. Moutinho, L.C. Peixoto, I.L. Ferreira, A. Garcia, Electrochim. Acta **56**, 8412–8421 (2011)
7. E.C. Araújo, A.S. Barros, R.H. Kikuchi, A.P. Silva, F.A. Gonçalves, A.L. Moreira, O.L. Rocha, Metall. Mater. Trans. A **48**, 1163–1175 (2017)
8. E. Sjölander, S. Seifeddine, J. Mater. Process. Technol. **210**, 1249–1259 (2010)
9. E.H. Samuel, A.M. Samuel, H.W. Doty, AFS Trans. **30**, 893–901 (1996)
10. A.M. Samuel, P. Ouellet, F.H. Samuel, H.W. Doty, AFS Trans. **105**, 951–962 (1997)
11. A.M. Samuel, J. Gauthier, F.H. Samuel, Metall. Mater. Trans. A **27**, 1785–1798 (1996)
12. Z. Li, A.M. Samuel, F.H. Samuel, C. Ravindran, S. Valtierra, J. Mater. Sci. **38**, 1203–1218 (2003)
13. Y.M. Han, A.M. Samuel, F.H. Samuel, S. Valtierra, H.W. Doty, AFS Trans. **116**, 79–90 (2008)
14. M.F. Ibrahim, E. Samuel, A.M. Samuel, A.M.A. Al-Ahmari, F.H. Samuel, Mater. Des. **32**, 2130–2142 (2011)
15. O.L. Rocha, C.A. Siqueira, A. Garcia, Metall. Mater. Trans. A **34**, 995–1006 (2003)
16. D. Bouchard, J.S. Kirkaldy, Metall. Mater. Trans. B **28**, 651–663 (1997)
17. J.D. Hunt, S.Z. Lu, Mater. Sci. Eng., A **173**, 79–83 (1993)
18. H. Kaya, U. Böyük, E. Çadırlı, N. Maraşlı, Mater. Des. **34**, 707–712 (2012)
19. R. Trivedi, Y.X. Shen, S. Liu, Metall. Mater. Trans. A **34**, 395–401 (2003)
20. E. Çadırlı, U. Böyük, S. Engin, H. Kaya, J. Alloys Compd. **694**, 471–479 (2017)
21. M. Gündüz, E. Çadırlı, Mater. Sci. Eng., A **327**, 167–185 (2002)
22. H. Kaya, E. Çadırlı, U. Böyük, N. Maraşlı, Appl. Surf. Sci. **255**, 3071–3078 (2008)
23. A.S. Barros, I.A. Magno, F.A. Souza, C.A. Mota, A.L. Moreira, M.S. Silva, O.L. Rocha, Metals Mater. Int. **21**, 429–439 (2015)
24. D.B. Carvalho, E.C. Guimarães, A.L. Moreira, D.J. Moutinho, J.M. Dias Filho, O.L. Rocha, Mater. Res. **16**, 874–883 (2013)
25. M.D. Peres, C.A. Siqueira, A. Garcia, J. Alloys Compd. **381**, 168–181 (2004)
26. O.L. Rocha, C.A. Siqueira, A. Garcia, Mater. Sci. Eng., A **361**, 111–118 (2003)
27. F. Sá, O.L. Rocha, C.A. Siqueira, A. Garcia, Mater. Sci. Eng., A **373**, 131–138 (2004)
28. C. Brito, T.A. Costa, T.A. Vida, F. Bertelli, N. Cheung, J.E. Spinelli, A. Garcia, Metall. Mater. Trans. A **46**, 3342–3355 (2015)
29. R. Chen, Q. Xu, H. Guo, Z. Xia, Q. Wu, B. Liu, Mater. Sci. Eng., A **685**, 391–402 (2017)
30. T.A. Costa, M. Dias, L.G. Gomes, O.L. Rocha, A. Garcia, J. Alloys Compd. **683**, 485–494 (2016)
31. A.J. Vasconcelos, R.H. Kikuchi, A.S. Barros, T.A. Costa, M. Dias, A.L. Moreira, A.P. Silva, O.L. Rocha, An. Acad. Bras. Ciênc. **88**, 1099–1111 (2016)
32. T.A. Costa, A.L. Moreira, D.J. Moutinho, M. Dias, I.L. Ferreira, J.E. Spinelli, O.L. Rocha, A. Garcia, Mater. Sci. Technol. **31**, 1103–1112 (2015)
33. D.J. Moutinho, L.G. Gomes, O.L. Rocha, I.L. Ferreira, A. Garcia, Mater. Sci. Forum **730–732**, 883–888 (2013)
34. M. Rappaz, W.J. Boettinger, Acta Mater. **47**, 3205–3219 (1999)
35. A. Sharma, Y.S. Shin, J. Jung, J. Weld. Join. **33**, 1–8 (2015)
36. R. Chen, Y. Shi, Q. Xu, B. Liu, Trans. Nonferrous Metals Soc. China **24**, 1645–1652 (2014)
37. T. Okamoto, K. Kishitake, J. Cryst. Growth **129**, 137–146 (1975)
38. W. Kalifa, A.M. Samuel, F.H. Samuel, H.W. Doty, S. Valtierra, Int. J. Cast Metal Res. **19**, 156–166 (2006)
39. J.A. Taylor, Proc. Mater. Sci. **1**, 19–33 (2012)
40. L. Liu, A.M.A. Mohamed, A.M. Samuel, F.H. Samuel, H.W. Doty, S. Valtierra, Metall. Mater. Trans. A **40**, 2457–2469 (2009)
41. M.A. Moustafa, J. Mater. Process. Technol. **209**, 605–610 (2009)
42. C.M. Dinnis, J.A. Taylor, A.K. Dahle, Metall. Mater. Trans. A **37**, 3283–3291 (2006)
43. C.M. Dinnis, J.A. Taylor, A.K. Dahle, Mater. Sci. Eng., A **425**, 286–296 (2006)
44. Z. Ma, A.M. Samuel, F.H. Samuel, H.W. Doty, S. Valtierra, Mater. Sci. Eng., A **490**, 36–51 (2008)
45. N. Roy, A.M. Samuel, F.H. Samuel, Metall. Mater. Trans. A **27**, 415–429 (1996)
46. C. Puncreobutr, P.D. Lee, K.M. Kareh, T. Connolley, J.L. Fife, A.B. Phillion, Acta Mater. **68**, 42–51 (2014)
47. M. Warmuzek, in *Aluminum–Silicon Casting Alloys: An Atlas of Microfractographs* (ASM International, Materials Park, 2004)
48. ASM International, *ASM Handbook: Volume 12: Fractography*, 9th edn. (ASM International, Metals Park, 1987)
49. K. Liu, X. Cao, X.-G. Chen, Metall. Mater. Trans. B **43**, 1231–1240 (2012)
50. A.M. Samuel, F.H. Samuel, J. Mater. Sci. **30**, 4823–4833 (1995)
51. A.M. Samuel, F.H. Samuel, H.W. Doty, S. Valtierra, Int. J. Metalcasting **11–3**, 552–567 (2017)
52. Z. Li, A.M. Samuel, F.H. Samuel, C. Ravindran, S. Valtierra, H.W. Doty, Mater. Sci. Eng., A **367**, 96–110 (2004)
53. P.R. Goulart, J.E. Spinelli, W.R. Osório, A. Garcia, Mater. Sci. A **421**, 245–253 (2006)
54. R.V. Reyes, T.S. Bello, R. Kakitani, T.A. Costab, A. Garcia, N. Cheung, J.E. Spinelli, Mater. Sci. Eng., A **685**, 235–243 (2017)
55. E. Çadırlı, Metals Mater. Int. **19**, 411–422 (2013)
56. A.T.R. Franco, C. Frajuca, F.Y. Nakamoto, G.A. dos Santos, A.A. Couto, Mater. Res. **21**, 1–8 (2018)